

Bioinspiration & Biomimetics



PAPER

Structure of tracheae and the functional implications for collapse in the American cockroach

RECEIVED
23 August 2015

REVISED
19 October 2015

ACCEPTED FOR PUBLICATION
23 October 2015

PUBLISHED
18 November 2015

Matthew R Webster¹, John J Socha², Luciano Teresi³, Paola Nardinocchi⁴ and Raffaella De Vita¹

¹ Mechanics of Soft Biological Systems Laboratory, Department of Biomedical Engineering and Mechanics, Virginia Tech, USA

² Comparative Biomechanics and Bio-Inspired Engineering Laboratory, Department of Biomedical Engineering and Mechanics, Virginia Tech, USA

³ Modelling and Simulation Lab, Department of Mathematics and Physics, Università Roma Tre, Rome, Italy

⁴ Department of Structural Engineering and Geotechnics, Sapienza Università di Roma, Rome, Italy

E-mail: devita@vt.edu

Keywords: trachea, American cockroach, SEM, collapse, microstructure, FEM

Abstract

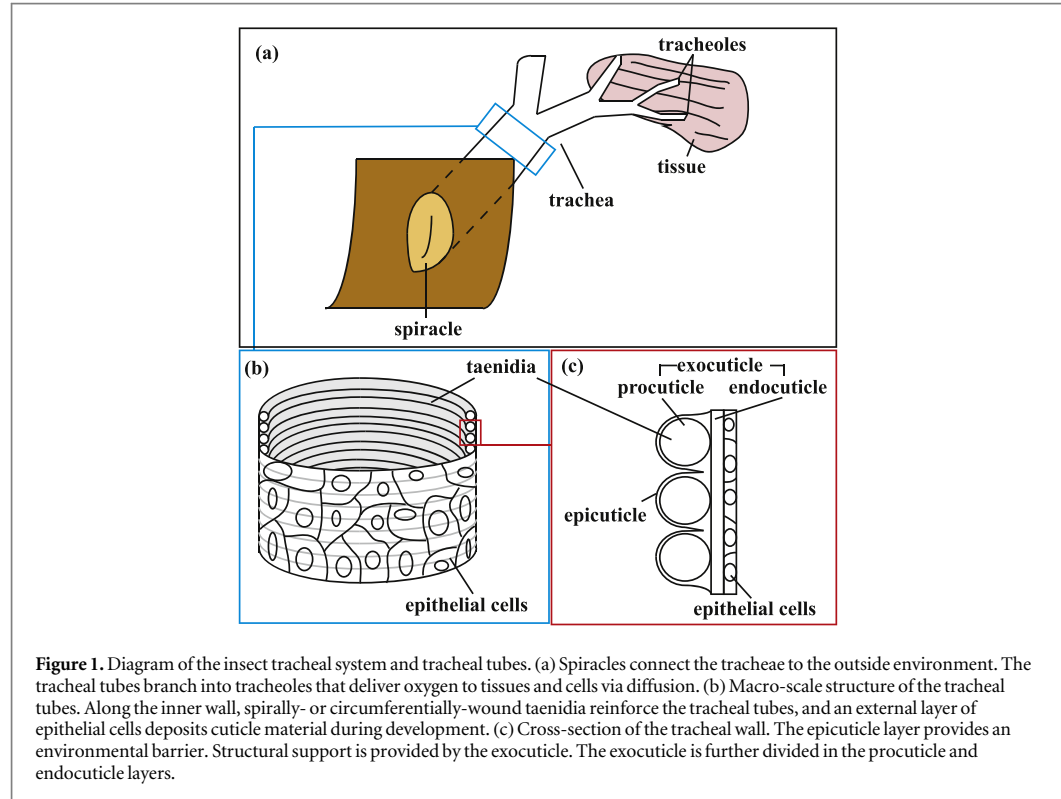
The tracheal tubes of insects are complex and heterogeneous composites with a microstructural organization that affects their function as pumps, valves, or static conduits within the respiratory system. In this study, we examined the microstructure of the primary thoracic tracheae of the American cockroach (*Periplaneta americana*) using a combination of scanning electron microscopy and light microscopy. The organization of the taenidia, which represents the primary source of structural reinforcement of the tracheae, was analyzed. We found that the taenidia were more disorganized in the regions of highest curvature of the tracheal tube. We also used a simple finite element model to explore the effect of cross-sectional shape and distribution of taenidia on the collapsibility of the tracheae. The eccentricity of the tracheal cross-section had a stronger effect on the collapse properties than did the distribution of taenidia. The combination of the macro-scale geometry, meso-scale heterogeneity, and microscale organization likely enables rhythmic tracheal compression during respiration, ultimately driving oxygen-rich air to cells and tissues throughout the insect body. The material design principles of these natural composites could potentially aid in the development of new bio-inspired microfluidic systems based on the differential collapse of tracheae-like networks.

1. Introduction

In the insect respiratory system, gas is transported through an intricate network of tracheal tubes. Insects intake gas from and expel gas to the ambient environment through valves known as spiracles located along the exoskeleton, and oxygen and carbon dioxide are exchanged directly with the tissues and cells at minute branches known as tracheoles via diffusion [1] (figure 1(a)). Some species supplement the diffusion of gas with advective flow driven by the periodic collapse and re-inflation of the tracheal tubes, a phenomenon known as rhythmic tracheal compression [2–6]. During tracheal compression, some tracheal tubes (or sections) serve as static conduits for the flow of gas, while others collapse and re-inflate, acting as either pumps to generate advective flows, or valves that could isolate sections of the tracheal system [7]. Although

active ventilation has been known to occur in insects for over a century [1, 8], the basis for differences in functional behavior of the tracheae has never been explored.

The tracheal tubes of insects, like the external exoskeletal cuticle, have a complex layered microstructure (figures 1(b) and (c)) consisting of an epicuticle that provides an environmental barrier and a chitin-reinforced exocuticle that provides structural support. The exocuticle can be further divided into the procuticle and the endocuticle. In the specialized tracheal tissue, the procuticle contains thickenings known as taenidia, whereas the endocuticle contains roughly parallel layers. These layers are helically stacked and rotated slightly relative to each other. The fibrous components of the tracheae are bound by a protein-rich component. A layer of epithelial cells on the outer surface of the tracheae is responsible for



producing secretions during growth and development, and this layer may also play an important role in the organization of the taenidia [9, 10].

The taenidia provide the primary source of structural reinforcement for the tracheae. Taenidia are typically described as spirally wound or ring-like thickenings, implying a high level of uniformity, yet variations in their organization have been noted. Wigglesworth [1] described the taenidia in the compressible tracheal tubes of the beetle *Dytiscus* and the mosquito *Culex* as 'tend[ing] to atrophy so that the tubes collapse when the pressure within them is reduced'. Similarly, Richards and Anderson [11] described the taenidia in the thoracic tracheae of the American cockroach (*Periplaneta americana*) as discontinuous helices.

The tracheae of the American cockroach were among the first tracheae to be examined with electron microscopy. However, Richards and Anderson [11] used methods for specimen preparation that are now known to alter the tissue microstructure, including drying in air. Moreover, they were only able to collect images for sections of tracheae that were sufficiently thin to allow electrons to pass through the detector of the microscope. Later, Richards and Korda [12] also analyzed sections of tracheae that were chemically treated for the removal of some protein components. Their study provided the first information about the organization of fibers in tracheal tubes, but the chemical treatment induced significant experimental

artifacts. Since these early studies, the structure of the primary thoracic tracheal tubes of the American cockroach has not been re-examined. Modern imaging methods and preparation techniques can greatly enhance our knowledge about the microstructure of these tracheae. They may reveal not only how such microstructure relates to their respiratory function, but also how it affects their material behavior, which has been recently characterized [13, 14].

The goal of this study was to provide a detailed description of the microstructure of the primary thoracic tracheae of the adult male American cockroach (*Periplaneta americana*). These tracheae can be considered 'compressible' because of their elliptical cross-sectional shape [1], but this remains an inference that has not been experimentally verified. We used scanning electron microscopy (SEM) and light microscopy to observe the different components of the tracheae, and to quantify the eccentricity of the cross-section and organization of the taenidia. In the process, we also observed the different layers of the tracheae and their interaction with the taenidia. Using a simple finite element model, we investigated the relationship between the geometrical and structural characteristics of the tracheae, particularly the eccentricity of the tracheal cross-section and the organization of the taenidia, and its collapse under a deflating pressure. Together our structural and computational study offers a new understanding of the material design of

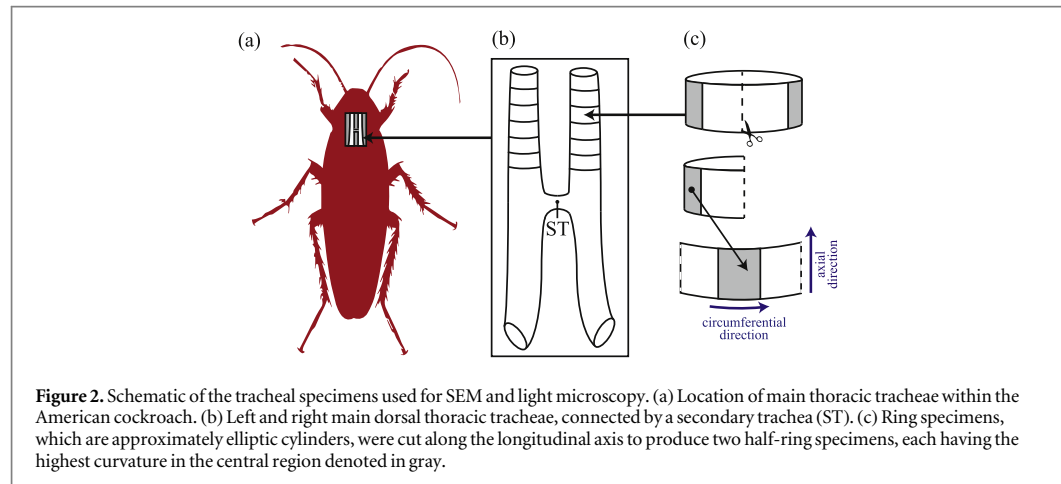


Figure 2. Schematic of the tracheal specimens used for SEM and light microscopy. (a) Location of main thoracic tracheae within the American cockroach. (b) Left and right main dorsal thoracic tracheae, connected by a secondary trachea (ST). (c) Ring specimens, which are approximately elliptic cylinders, were cut along the longitudinal axis to produce two half-ring specimens, each having the highest curvature in the central region denoted in gray.

insect tracheal tubes as it relates to their function during respiration.

2. Materials and methods

We first examined the microstructure of the primary thoracic tracheae of the American cockroach using SEM. Our SEM analysis revealed the main structural components of the tracheae, including local variations in the organization of the taenidia. Because the specimens were dried for such analyses, they became brittle and more prone to damage during handling. For this reason, the organization of the taenidia along the tracheal circumferential direction was quantified using conventional light microscopy. Specimens that were viewed using light microscopy did not require extensive preparation and were not dried, and their position under the microscope was easily adjusted without inducing damage. Moreover, due to the low cost associated with specimen preparation, a larger number of tracheae could be analyzed.

2.1. Specimen dissection

Adult male American cockroaches (*Periplaneta americana*; $n = 13$) of mass 0.7686 ± 0.135 g (mean \pm S.D.) and length 33.7 ± 1.7 mm were obtained from a colony in the Department of Entomology at Virginia Tech. The insects were sacrificed with fumes of ethyl acetate, and the primary thoracic tracheal trunks were removed by dissection (figure 2(a)) and placed immediately in a bath of insect Ringer's solution (0.75 g NaCl, 0.035 g KCl, 0.021 g CaCl₂, 100 ml distilled water [15]) to maintain hydration. The primary thoracic tracheae from 8 insects were analyzed using SEM, and those from 5 insects were analyzed using light microscopy. A total of 32 tracheae, which included 13 dorsal left, 11 dorsal right, 4 ventral left, and 4 ventral right tracheae, were extracted.

2.2. SEM: specimen preparation

A total of 23 thoracic tracheae were examined using SEM. These include 8 dorsal left, 7 dorsal right, 4 ventral left, and 4 ventral right tracheae. The tracheae were fixed in a solution of 5% glutaraldehyde in 0.1 M sodium cacodylate buffer for 24 h, post-fixed in 1% osmium tetroxide in a sodium cacodylate buffer for 1 h, and then washed in the same buffer for 10 min. The tracheae were then dehydrated in a graded series of ethanol treatments (15%, 30%, 50%, 70%, 95%, and 100%, respectively) and dried in a critical-point dryer (Model 28000; LADD Research Industries; Williston, Vermont, United States). Double-sided tape was used to attach the dried tracheae to SEM stages, where they were then coated with gold using a modular sputter coater (Model 11430; Structure Probe Inc.; West Chester, Pennsylvania, United States). Different specimens were used to analyze various features of the tracheal structure. Intact dorsal and ventral tracheae ($n = 2$ of each) were used to analyze the macro-scale geometry of the tracheae and the outer layer of their walls. Tracheae bisected along the longitudinal direction ($n = 15$) were used to study the cross-section and intima layer of their walls. Finally, tracheae that were manually fractured with forceps ($n = 6$) were used to determine the inner structure of the tracheal wall. Images were taken using a SEM (EVO40 SEM; Carl Zeiss; Jena, Germany) with an excitation voltage ranging from 10 kV to 20 kV, a working distance of 5 mm, and magnifications ranging from $100\times$ to $50\,000\times$.

2.3. SEM: image analysis

Length and angle measurements were obtained from SEM images using ImageJ software (National Institute of Health; Bethesda, Maryland, United States) [16]. These measurements were only performed on SEM images from specimens that were deemed free of any obvious damage resulting from the preparation process. The thickness of the taenidia was measured from one image of the wall of the tracheae in 15 locations

where the cross-section of the taenidia alone was clearly visible. The thickness of the entire tracheal wall was measured in 6 locations where the outer layers of the tissue were flat against the taenidia. The diameter of papillae that were observed in one image of the inner surface of the tracheae was measured in 15 locations. Measurements were only taken from papillae that had an approximately circular shape. Mean values and standard deviations were calculated from all measurements.

2.4. Light microscopy: specimen preparation

Nine thoracic tracheae (5 dorsal right and 4 dorsal left) were used to determine the shape of their cross-sections and the number of taenidia along the circumferential direction. These tracheae were anterior to the secondary trachea that connects the left and right dorsal thoracic tracheae (figure 2(b)). The tracheae were sectioned in roughly uniform rings, each having approximately the shape of an elliptical cylinder (figure 2(c)). These ring sections ($n = 36$) were placed on a 1 mm optical grid (Edmund Optics LTD; York, United Kingdom) under a dissection microscope (Stemi 2000 C Stereo Microscope; Carl Zeiss; Jena, Germany) oriented with the longitudinal axis of the trachea aligned with the optical axis of the microscope to visualize the cross-section. Images of the cross-sections were collected at $5\times$ magnification using an SLR camera (D5000; Nikon Corporation; Tokyo, Japan) attached to the microscope. Each ring specimen was then cut along the longitudinal direction so as to produce two half-ring specimens ($n = 72$), each with the region of highest curvature approximately in the center (figure 2(c)). The half-ring sections ($n = 72$) were laid flat on a microscope slide, and transparent double-sided tape was laid on top for adherence. Images of these sections were collected at $10\times$ magnification using an inverted microscope (IX-51 Inverted Microscope; Olympus Corporation; Tokyo, Japan) equipped with a digital camera (Model DCC1645C; Thorlabs Inc.; Newton, New Jersey, United States).

2.5. Light microscopy: image analysis

Prior to analyzing images gathered via light microscopy, magnification factors were calculated using images of a $50\ \mu\text{m}$ optical grid (Thorlabs Inc.; Newton, New Jersey, United States) as a reference. These factors were used to convert measurements from pixel units to physical units. The images of the cross-sections of the ring sections ($n = 36$) were analyzed to determine their geometrical shape using ImageJ. The cross-sections were first traced by manually selecting points along their arc-length. For each cross-section, the maximum distance between two points was computed. This distance was then used to normalize the coordinates of the points that defined the cross-section. The traces of all the cross-sections were

plotted together in the x - y Cartesian coordinate system with the normalized segments of maximum distances oriented along the x -axis and centered at the origin (0, 0). The canonical equation of an ellipse, $(x/a)^2 + (y/b)^2 = 1$ where $a = 0.5$ and b are the semi-major and semi-minor axes, respectively, was then fit to the set of data points that represented the cross-sections using the least-squares method in Matlab (MATLAB and Statistics Toolbox Release 2012b, The MathWorks, Inc.; Natick, Massachusetts, United States) to determine the value of b .

The images of the half-ring sections ($n = 72$) were analyzed using ImageJ to quantify the change in the number of taenidia along the circumferential direction. More precisely, the number of taenidia for each half-ring section was calculated at one of the two axial edges by counting the points of intersection of the taenidia with a straight line oriented in the axial direction. Upon inspection of the initial specimens, we noticed that some taenidia bifurcated along the circumference. The locations of each bifurcation point was identified. Consequently, changes in the number of taenidia were quantified at the point where a single taenidium branched into two, or where two taenidia fused into one. To compare changes in the number of taenidia across the 72 half-ring sections with different circumferential lengths, the circumferential coordinate of each half-ring section was normalized by its half-circumferential length and multiplied by π to convert to angular units. Similarly, the number of taenidia, $N(\theta)$, as a function of the normalized circumferential coordinate, θ , for each half-ring section was normalized by the maximum number of taenidia observed along its circumferential length, $N_{\max} = \max(N(\theta))$, for $0 \leq \theta \leq \pi$.

2.6. Finite element model

The tracheal tube was modeled as a nonlinear three-dimensional solid having the shape of a thin elliptical cylinder. The St. Venant–Kirchhoff constitutive model was used to capture the nonlinear elastic behavior of the tracheae. More specifically, the second Piola–Kirchhoff tensor, \mathbf{S} , was assumed to have the following form [17]:

$$\mathbf{S}(\mathbf{E}) = \frac{Y}{(1 + \nu)}\mathbf{E} + \nu \frac{Y}{(1 + \nu)(1 - 2\nu)} \text{tr}(\mathbf{E})\mathbf{I}, \quad (1)$$

where $\mathbf{E} = \frac{1}{2}(\mathbf{F}^T\mathbf{F} - \mathbf{I})$ is the Green–Lagrangian strain tensor, $\mathbf{F} = \mathbf{I} + \nabla\mathbf{u}$ is the deformation gradient tensor, \mathbf{I} is the identity tensor, and \mathbf{u} is the displacement field. Y and ν are the Young’s modulus and the Poisson ratio of the tracheal tubes, respectively. They were set as $Y = 1.7\ \text{GPa}$ and $\nu = 0.3$, based on our previous studies on tracheal material properties [13, 14]. The tube’s length was set to $L = 4\ \text{mm}$, the thickness to $t = 4\ \mu\text{m}$, and the semi-major axis to $a = 400\ \mu\text{m}$. The tracheal tube was assumed to be clamped at both ends.

The mechanical behavior of the tube under a negative inner pressure was studied in order to understand

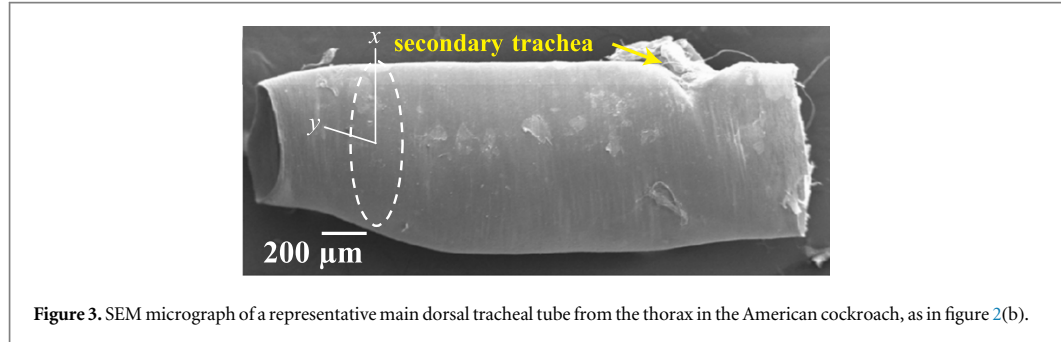


Figure 3. SEM micrograph of a representative main dorsal tracheal tube from the thorax in the American cockroach, as in figure 2(b).

its collapse behavior. In particular, the buckling pressure was determined. This was defined as the pressure at the onset of the first major collapse of the tube. The associated post-buckling configuration, which is the shape assumed by the tube for a pressure above the buckling pressure, was also analyzed. A pressurization test, which consists of a sequence of stationary problems with increasing applied pressure p_i for $i = 1, \dots, n$, with $p_1 = 0.2$ kPa, $p_n = 7$ kPa, and $p_{i+1} - p_i = 0.02$ kPa, was solved by using a continuation strategy. By following this strategy, which is typically used for nonlinear problems [18], the solution found for each pressure p_i was used as the initial guess for the search of the solution corresponding to the pressure p_{i+1} .

To analyze the effect of the cross-sectional eccentricity of the tracheal tube on the buckling pressure, the pressurization test was solved for different values of the major to minor semi-axes ratio a/b . The values of a/b were selected to vary from 1.04 to 1.24 based on the results of the light microscopy study. The effect of the non-homogeneous organization of the taenidia along the circumferential direction on the buckling pressure was studied by solving the pressurization test with a varying Young's modulus of the form $Y(\theta) = Y(1 + \Delta(\cos^2 \theta - 1))$, where θ denotes the radial coordinate, $Y = 1.7$ GPa, and $\Delta = 1 - Y_{\min}/Y_{\max}$, with Y_{\min} and Y_{\max} representing the minimum and the maximum values of $Y(\theta)$, respectively. The origin of radial coordinate was chosen so that Y_{\min} occurred at the points of maximum curvature, as determined by the experimental data. The cross-section was assumed to be either elliptical with $a/b = 1.2$, or almost circular with $a/b = 1.04$. Then, the pressurization test was solved for each value of Δ_i , for $i = 1, \dots, n$, with $\Delta_1 = 0$, $\Delta_n = 0.3$, and $\Delta_{i+1} - \Delta_i = 0.05$.

The computational problem was implemented and solved using the finite element method with COMSOL Multiphysics (COMSOL Multiphysics Version 4.0). Tetrahedral elements and quadratic shape functions totaling approximately 450 000 degrees of freedom were used. More specifically, only one tetrahedral element along the thickness of the trachea was used. The resulting algebraic problem was solved through the direct solver MUMPS [35].

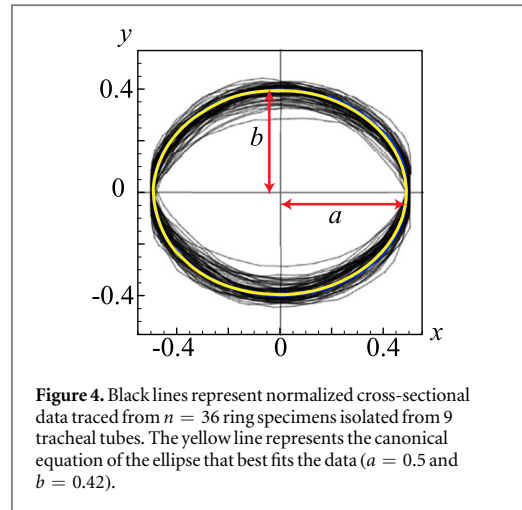


Figure 4. Black lines represent normalized cross-sectional data traced from $n = 36$ ring specimens isolated from 9 tracheal tubes. The yellow line represents the canonical equation of the ellipse that best fits the data ($a = 0.5$ and $b = 0.42$).

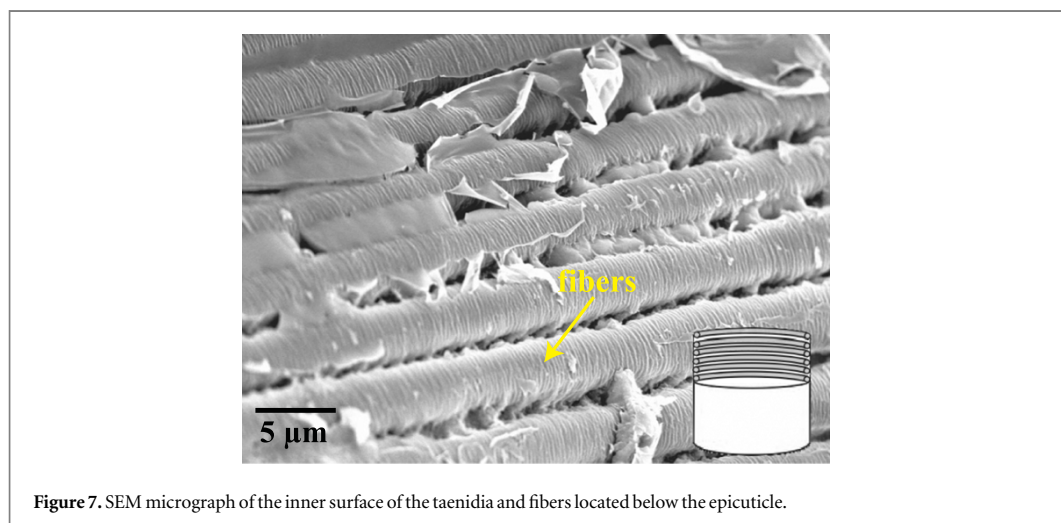
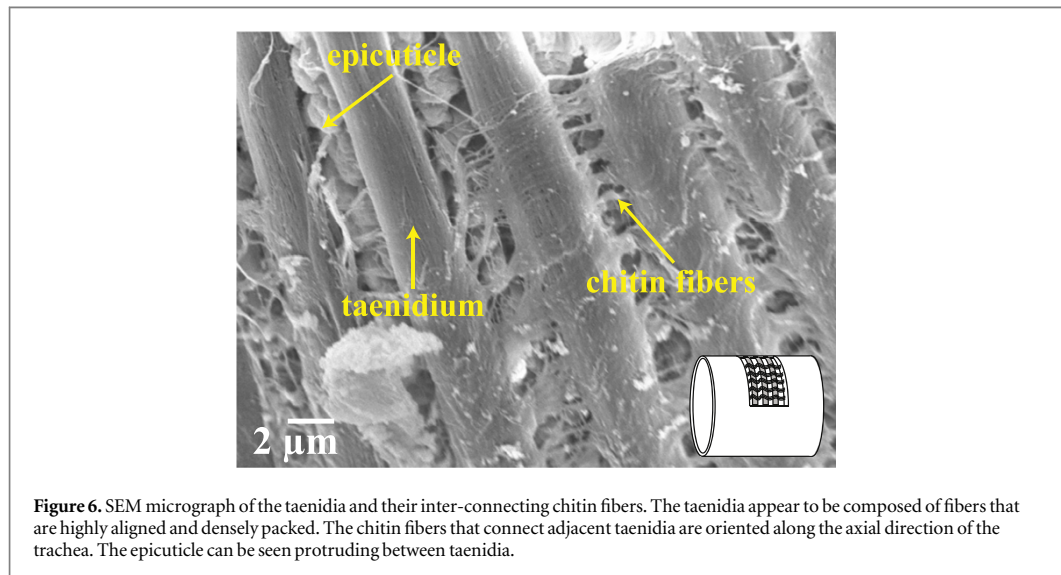
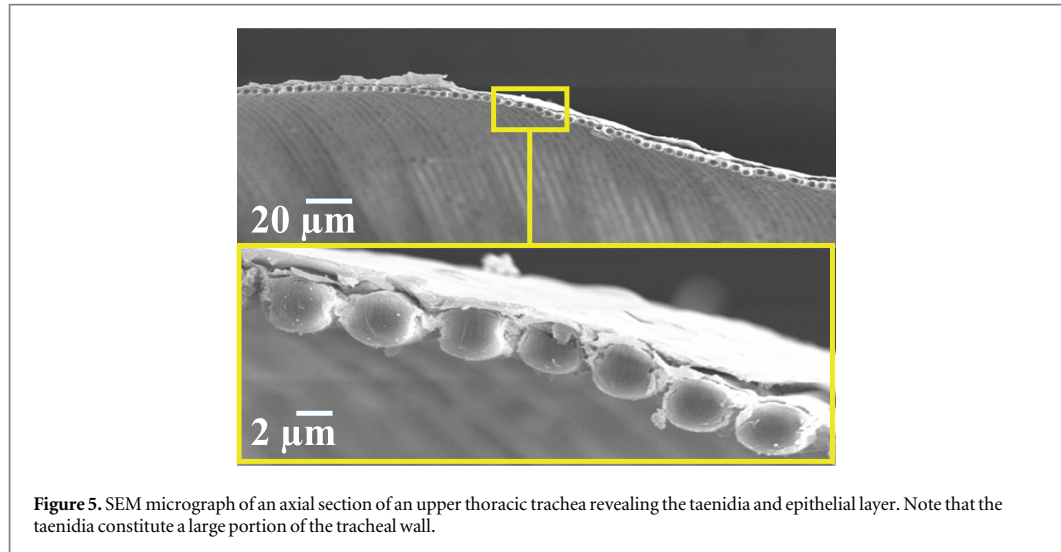
3. Results

3.1. SEM and light microscopy

The primary thoracic tracheae of the American cockroach were found to have an elliptical cross-section. The major and minor axes of these cross-sections increased near the region where the left and right tracheal tubes were connected by a secondary tracheal branch (figure 3). For the canonical equation of the ellipse, $(x/a)^2 + (y/b)^2 = 1$ with $a = 0.5$, the best-fit value of b computed from the normalized cross-sectional data for the $n = 36$ ring specimens was $b = 0.42$ (figure 4). Thus, the ratio of major to minor semi-axes a/b was determined to be 1.19 and the eccentricity $e = \sqrt{1 - (b/a)^2}$ was found to be 0.54.

The taenidia constituted the major component of the tracheal wall, which was clearly visible in SEM images (figure 5). From the specimen shown in this figure, the thickness (mean \pm S.D.) of the taenidia was determined to be $3.38 \pm 0.14 \mu\text{m}$ and the total thickness (mean \pm S.D.) of the tracheal wall was $3.88 \pm 0.38 \mu\text{m}$. From these measurements, the taenidia were estimated to make up 85% of the entire tracheal wall.

Fibers within each taenidium were observed to be densely packed and relatively straight (figure 6). The network of taenidia was connected on their outermost



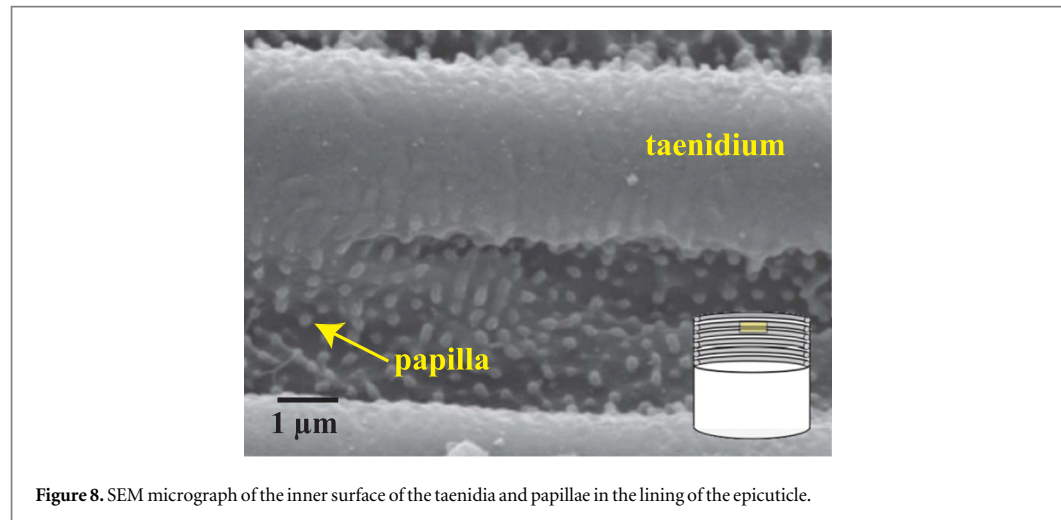


Figure 8. SEM micrograph of the inner surface of the taenidia and papillae in the lining of the epicuticle.

surface by a set of wavy chitin fibers oriented nearly perpendicularly to the direction of the taenidia, along the axial direction of the trachea (figure 6).

Fibers were also observed on the inner surface of the taenidia, adjacent to the epicuticle. These fibers were aligned in the axial direction of the tracheae and closely followed the contours of the wall (figure 7). However, it must be noted that these axially aligned fibers were not always observed beneath the epicuticle. For example, in figure 8, such fibers could not be detected, and instead minute papillae with a mean diameter of $0.16 \pm 0.02 \mu\text{m}$ were noted on the inner surface of the taenidia.

In the endocuticle, between the taenidia and the layers of epithelial cells of the tracheae, a meshwork of wavy fibers was observed and the fibers formed an angle of roughly 50° with the taenidia (figure 9). Another specimen reveals fibers with multiple orientations (figure 10).

Branching and fusion of the taenidia (i.e., bifurcation) were observed. Within the same tracheal walls, there were regions containing straight and parallel taenidia but also regions containing bifurcated and misaligned taenidia. For example, in one specimen the taenidia appeared to diverge from an ordered region, with a misalignment of up to 10° about their ordered alignment (figure 11). Clusters of branched taenidia within tracheal walls were also observed (figure 12). In the region shown between the dotted lines in figure 12, the number of taenidia decreased by roughly 14% and then increased by nearly the same amount.

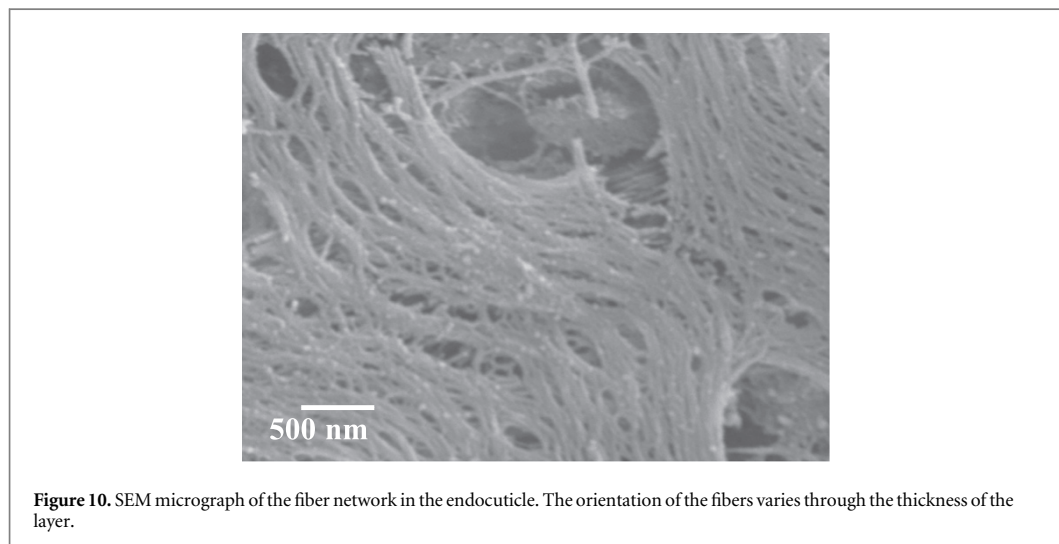
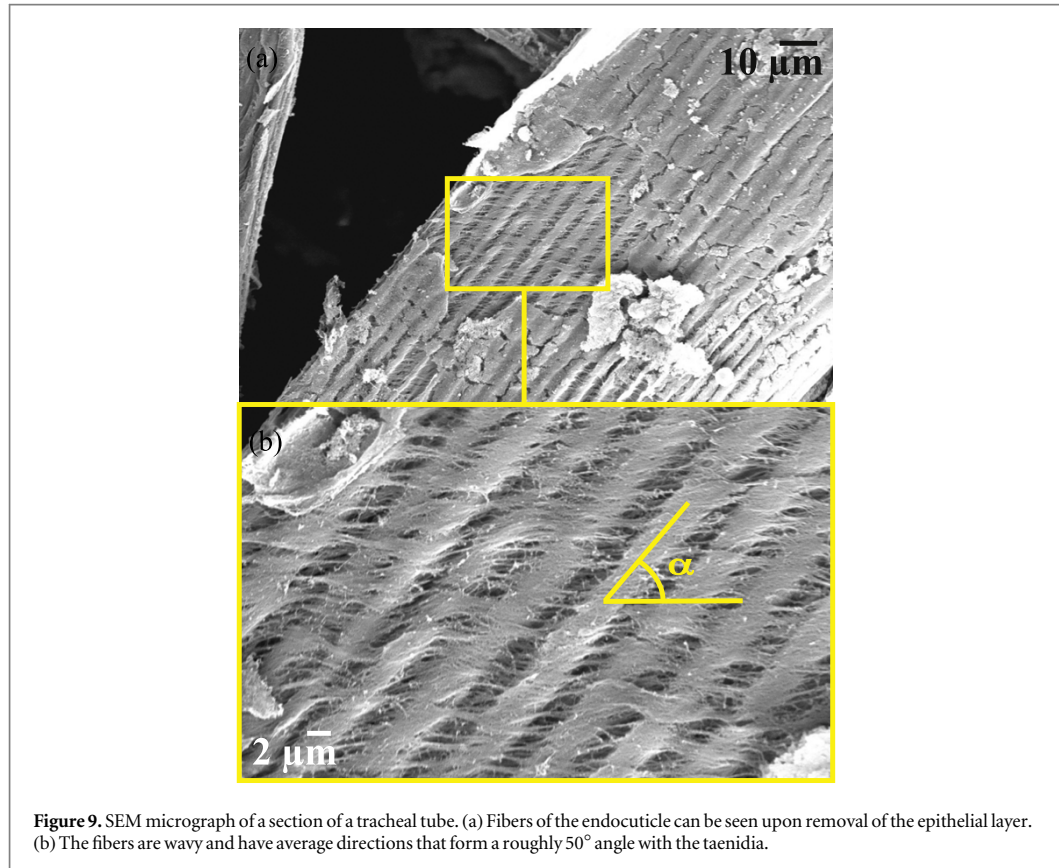
The location of bifurcated/fused taenidia along the circumferential direction of the tracheae was determined by analyzing the images of the half-ring sections collected using light microscopy. In the representative half-ring section shown in figure 13, the region of highest curvature contained an increased number of bifurcations. More specifically, the number of taenidia at $\theta = \pi/2$ was found to be $N(\pi/2) \approx 0.8N_{\text{max}}$. In other words, there was roughly a 20%

reduction in the maximum number of taenidia N_{max} . By collectively analyzing $n = 72$ half-ring sections, we found that, in the region of highest curvature at around $\theta = \pi/2$, the ratio of the local number of taenidia to the maximum number of taenidia was $N(\pi/2)/N_{\text{max}} = 88\% \pm 1\%$ (figure 14).

3.2. Finite element modeling

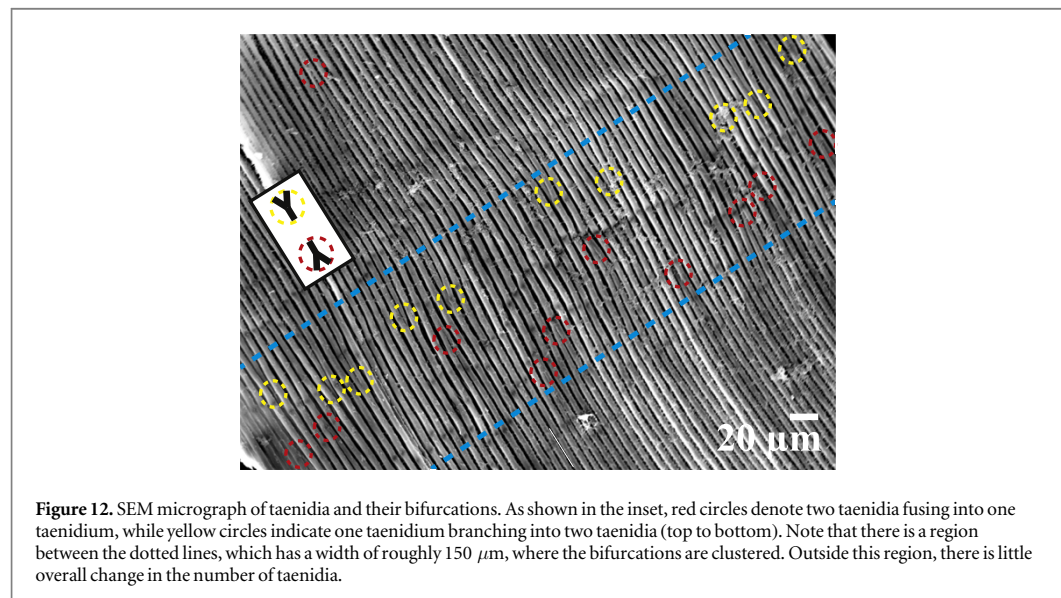
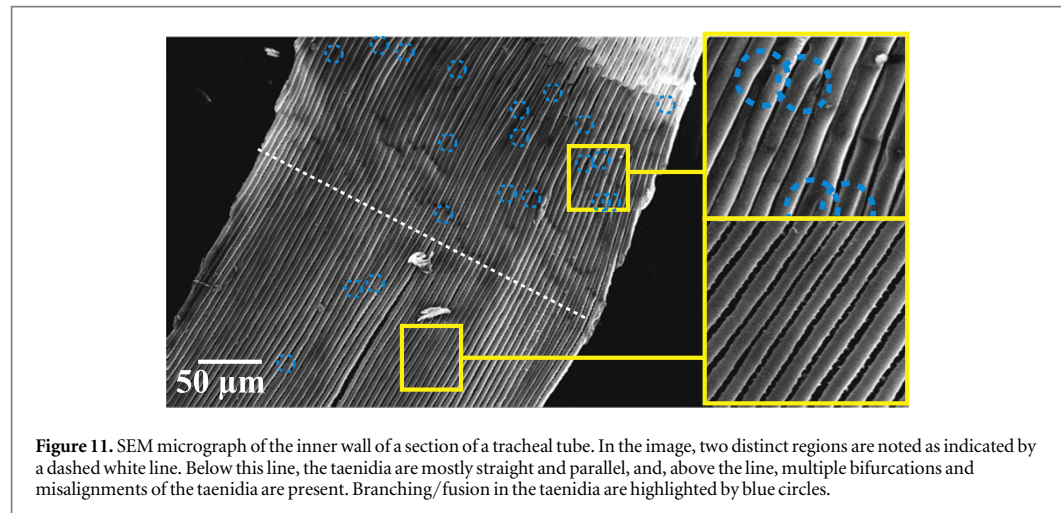
Numerical results on the effect of cross-sectional eccentricity on the pressure that causes collapse are reported in figure 15. The relative volume change of the tracheal tube, which is the change in volume over the initial volume, due to internal pressure was computed for different values of a/b . Jump discontinuities in the relative volume change versus pressure curves indicated the occurrence of buckling (figure 15(a)). Together with the undeformed configurations, the deformed configurations that illustrate the cross-sectional shape of the tube pre- and post-buckling are presented for $a/b = 1.2$ in figure 15(b) where $p = 3.8 \text{ kPa}$, figure 15(c) where $p = 4.0 \text{ kPa}$, figure 15(d) where $p = 7 \text{ kPa}$. These configurations are presented for $a/b = 1.04$ in figure 15(e) where $p = 7 \text{ kPa}$. The post-buckling configuration of the tracheal tubes was found to be similar for tracheae with elliptical cross-sections, across eccentricities. However, the post-buckling configuration was different for the near circular cross-section, where $a/b = 1.04$, as can be seen in figure 15(e). The typical post-buckling configuration is presented for a half tracheal tube in figure 15(f) for a constant negative internal pressure $p = 7 \text{ kPa}$ and $a/b = 1.2$. Buckling pressures were numerically computed for tracheal cross-sections with different eccentricity and, thus, different values of a/b (figure 15(g)). These numerical data show that a 16% increase in a/b , from 1.04 to 1.2, lowered the buckling pressure by 1.4 kPa (figure 15(g)).

The results of the numerical experiments on the influence of the circumferential variation of the



Young's modulus on the buckling pressure are shown in figure 16. The relative volume change of the tracheal tube due to internal pressure was computed for different values of Δ for both elliptical and almost circular cross-sections (figures 16(a) and (b)). Again, jump discontinuities in the relative volume change versus pressure curves marked the occurrence of buckling. We

analyzed the effect of a large (30%) circumferential variation of the Young's modulus on the collapse of a tracheal tube with $a/b = 1.20$ (figures 16(c)–(e)). Buckling of a tracheal tube with a non-homogeneous Young's modulus ($Y(\theta) = Y(1 + \Delta(\cos^2\theta - 1))$ with $Y = 1.7$ GPa, and $\Delta = 0.3$) occurred at a lower pressure than buckling of a tracheal tube with a

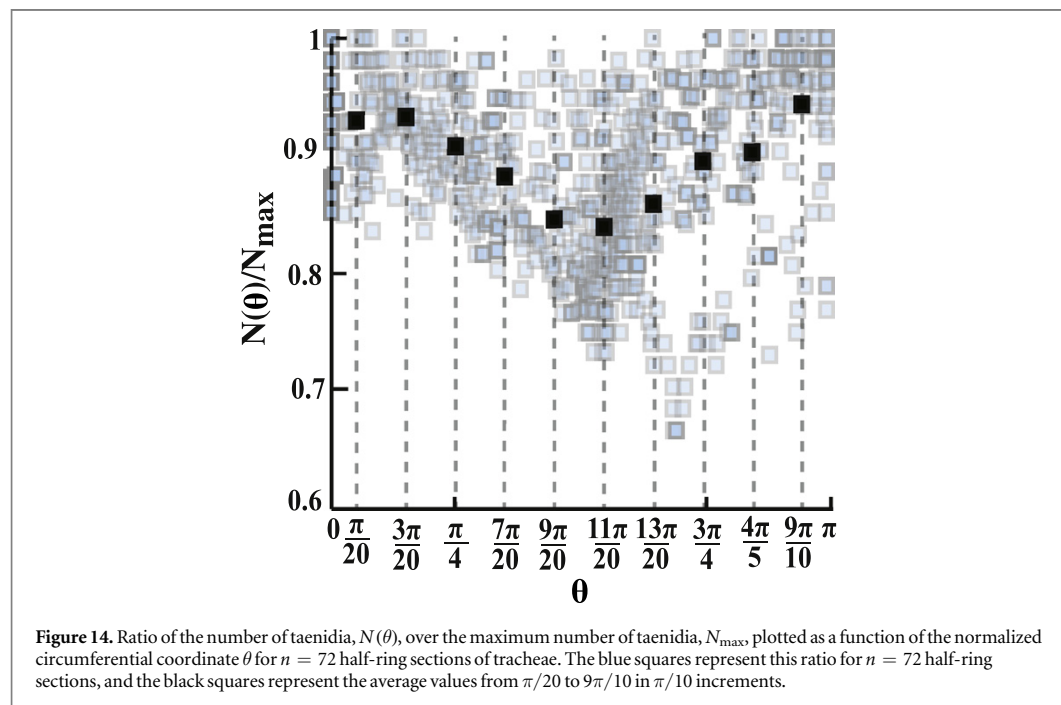
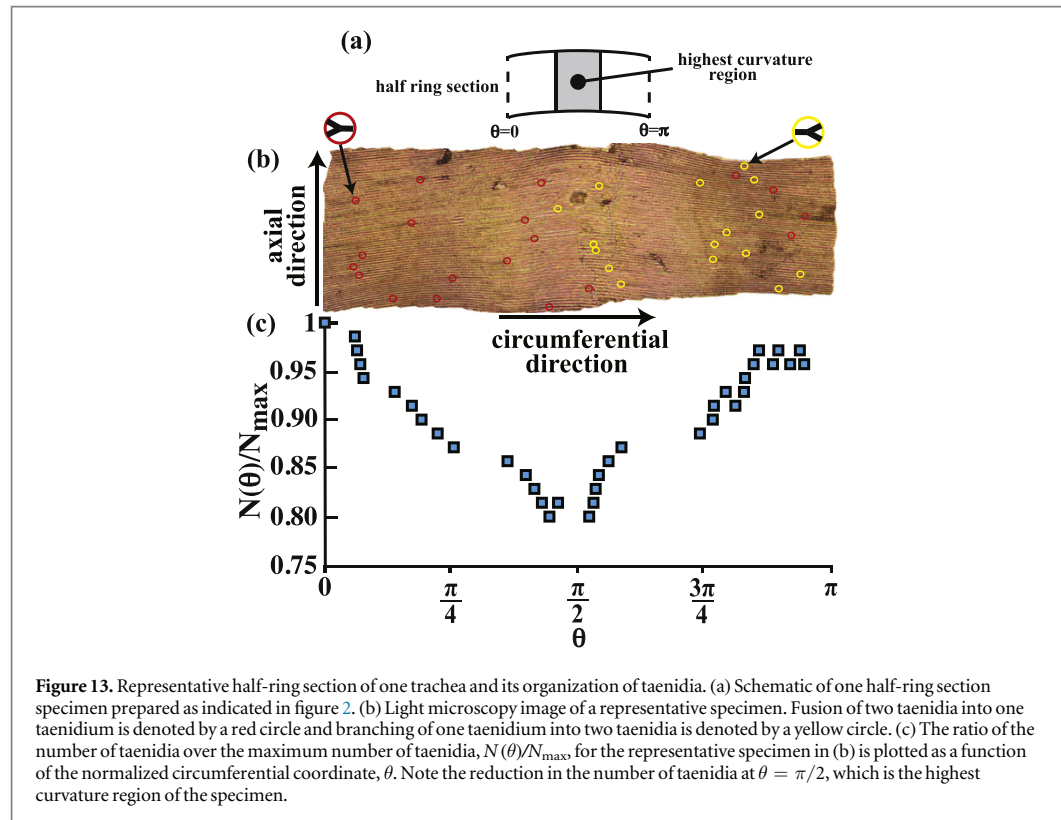


homogeneous Young's modulus (figure 16(c)). The post-buckling configurations of these tracheae were similar, although the amount of buckling was slightly larger for the tracheal tube with a non-homogeneous Young's modulus (figures 16(d) and (e)). The typical post-buckling configuration and the variation in Young's modulus are presented in figure 16(f) for a half tracheal tube. We found that the variation in the Young's modulus reduced the buckling pressure only slightly for an elliptical cross-section with $a/b = 1.2$, and that such a reduction was larger for an almost circular cross-section with $a/b = 1.04$ (figure 16(g)). Our results indicated that the change in Young's modulus affected the buckling pressure for an elliptical cross-section only if the reduction in Young's modulus was very large, up to 30% (i.e., $\Delta = 0.3$). As shown in figure 16(g), a 30% decrease in the Young's modulus lowered the buckling pressure by approximately 0.5 kPa when $a/b = 1.2$.

4. Discussion

This study provided an in-depth micro-structural characterization of the primary thoracic tracheae of the American cockroach. Our major findings about such microstructure are summarized in figure 17. In addition to obtaining a level of detail in our visualization that surpasses early studies [11, 12], we found a potentially important, yet unexplored, aspect of the microstructure of the tracheal wall: the circumferential organization of the taenidia, which demonstrated non-randomly distributed bifurcations. By using a finite element model, we showed that the eccentricity of the cross-section together with the circumferential organization of the taenidia play a crucial role in the collapse of the tracheae.

Not surprisingly, we found similarities between the microstructure of these tracheae and the tracheae of previously studied species, the adult Chinese silk



moth (*Antheraea pernyi*) [19] and the adult flesh fly (*Sarcophaga bullata*) [20]. Specifically, we confirmed that the taenidia were the primary source of reinforcement of the tracheal wall. According to our measurements, they constituted more than 80% of the wall

thickness of the tracheae (figure 17(a)). Adjacent to the taenidia, we observed fibers that were aligned along the axial direction of the trachea (figures 17(c) and (d)). These appeared to connect the taenidia and should therefore limit the axial deformation of the

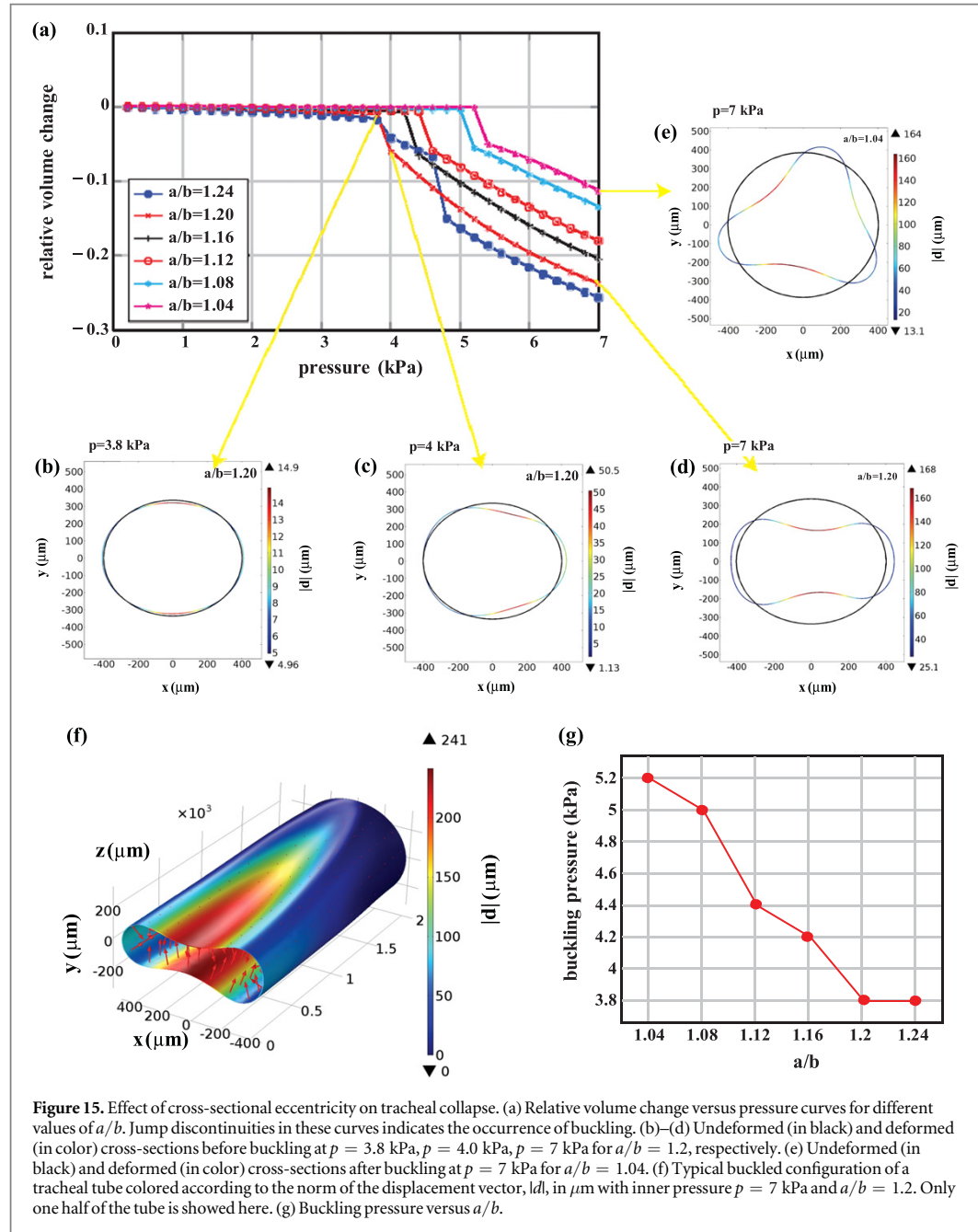


Figure 15. Effect of cross-sectional eccentricity on tracheal collapse. (a) Relative volume change versus pressure curves for different values of a/b . Jump discontinuities in these curves indicates the occurrence of buckling. (b)–(d) Undeformed (in black) and deformed (in color) cross-sections before buckling at $p = 3.8$ kPa, $p = 4.0$ kPa, $p = 7$ kPa for $a/b = 1.2$, respectively. (e) Undeformed (in black) and deformed (in color) cross-sections after buckling at $p = 7$ kPa for $a/b = 1.04$. (f) Typical buckled configuration of a tracheal tube colored according to the norm of the displacement vector, $|d|$, in μm with inner pressure $p = 7$ kPa and $a/b = 1.2$. Only one half of the tube is shown here. (g) Buckling pressure versus a/b .

tracheal tubes. A meshwork of fibers was observed in the endocuticle (figure 17(e)) beneath the epithelial layer of the tracheae (figure 17(f)). Our description of the endocuticle with a meshwork of fibers is consistent with the description provided by Richards and Korda [12]. In their early study, the fibers in the endocuticle were only observed after dissolving some protein components of the tracheae. For this reason, the authors were unable to determine whether these fibers were formed by the protein removal process or if they were present in the intact tracheae. In our study, the intact tracheae were visualized without dissolving any of the

protein components, and the presence of a network of fibers in the endocuticle was positively identified.

There are limitations in the quantitative information that can be gained from our SEM and light microscopy analyses. These limitations stem primarily from artifacts that are induced by specimen preparation and examination. Some shrinking of the specimens likely occurred as a result of the critical point drying procedure used for SEM. Indeed, although the critical point drying method represents a major improvement over the air-drying method used in previous studies [11], alterations of the microstructure of the tracheae were

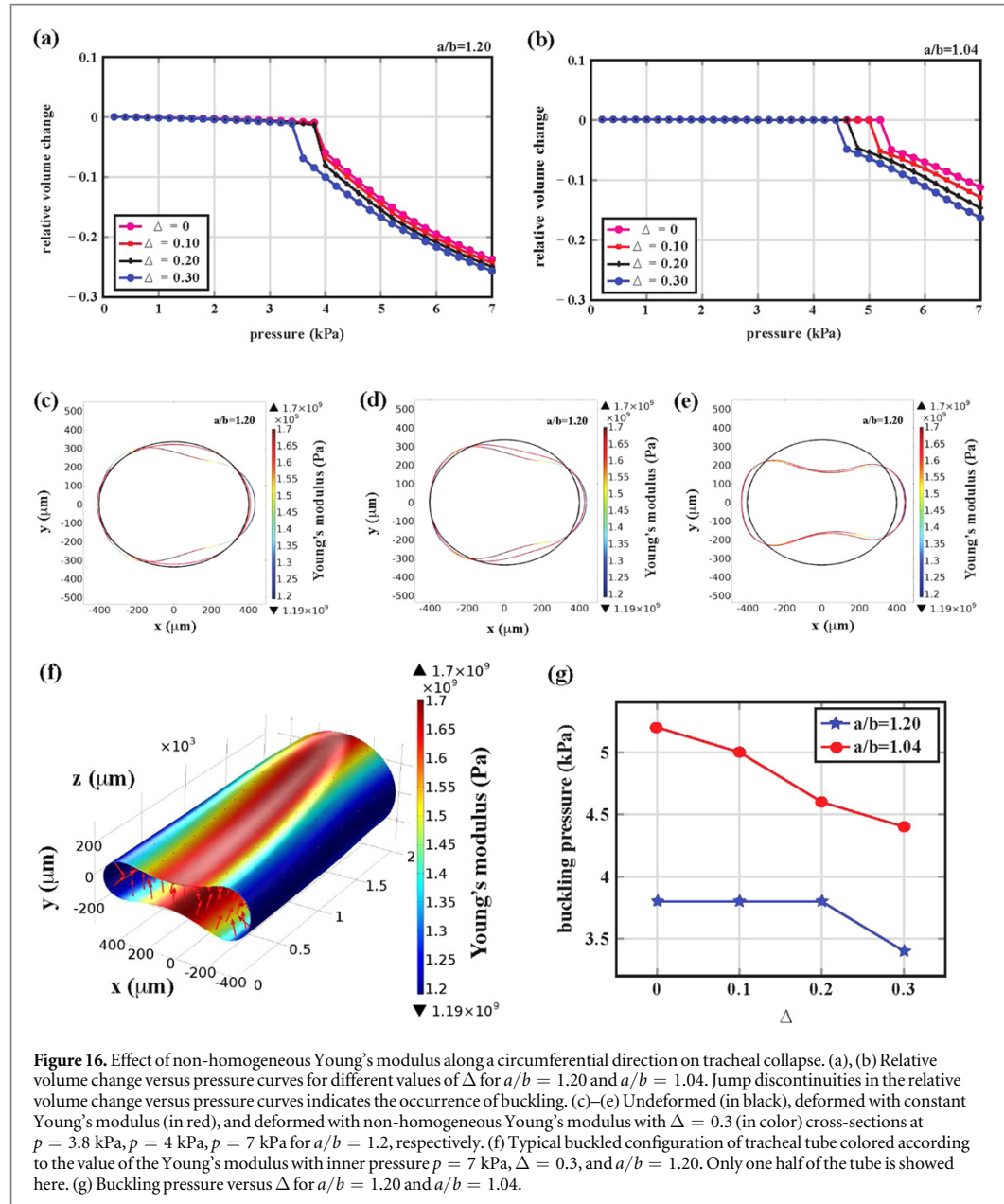


Figure 16. Effect of non-homogeneous Young's modulus along a circumferential direction on tracheal collapse. (a), (b) Relative volume change versus pressure curves for different values of Δ for $a/b = 1.20$ and $a/b = 1.04$. Jump discontinuities in the relative volume change versus pressure indicates the occurrence of buckling. (c)–(e) Undeformed (in black), deformed with constant Young's modulus (in red), and deformed with non-homogeneous Young's modulus with $\Delta = 0.3$ (in color) cross-sections at $p = 3.8$ kPa, $p = 4$ kPa, $p = 7$ kPa for $a/b = 1.2$, respectively. (f) Typical buckled configuration of tracheal tube colored according to the value of the Young's modulus with inner pressure $p = 7$ kPa, $\Delta = 0.3$, and $a/b = 1.20$. Only one half of the tube is showed here. (g) Buckling pressure versus Δ for $a/b = 1.20$ and $a/b = 1.04$.

inevitable and increased the uncertainty of our results [21]. For example, when comparing the thickness of the taenia to the thickness of the different layers of the tracheal wall, we assumed that shrinking occurred equally among all the components of the tracheae. However, it is quite possible that, during the critical point drying process, the taenia were less susceptible to changes in structure due to their high density compared to the endocuticle and epithelial layers. Even in our light microscopy analysis, which involved far less artifacts than those associated with SEM tissue preparation, there were unavoidable forces applied to the tracheae that could have altered their structure. These include shear forces applied during adhesion of tissue specimens to the microscope slides, and surface

tension forces applied by the Ringer's solution that was used to keep the specimens hydrated.

The collapse of the tracheae during active ventilation has historically been attributed to their elliptical cross-section [8]. Indeed, it is well known that a lower pressure is needed to induce collapse in an elliptical cylinder than in a perfectly circular cylinder, all else being equal [22]. Under the simplifying assumptions made about the geometry, boundary conditions, and material properties of the tracheae, our finite element simulations of the tracheae also revealed this pattern (figure 15). The simulations showed that collapse always occurred in the minor axis regions of the elliptical cross-sections (figures 15(b)–(f)). On the other hand, material defects are also known to influence the

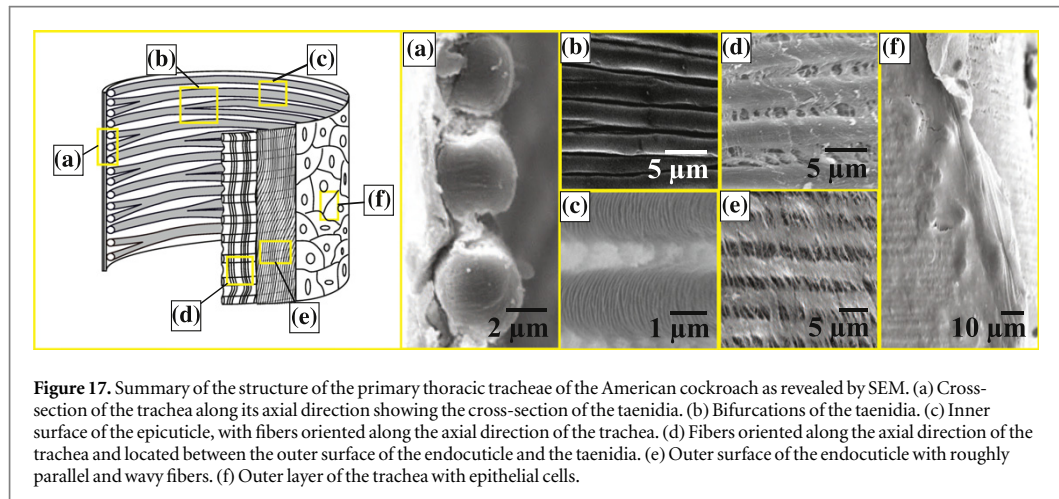


Figure 17. Summary of the structure of the primary thoracic tracheae of the American cockroach as revealed by SEM. (a) Cross-section of the trachea along its axial direction showing the cross-section of the taenidia. (b) Bifurcations of the taenidia. (c) Inner surface of the epicuticle, with fibers oriented along the axial direction of the trachea. (d) Fibers oriented along the axial direction of the trachea and located between the outer surface of the endocuticle and the taenidia. (e) Outer surface of the endocuticle with roughly parallel and wavy fibers. (f) Outer layer of the trachea with epithelial cells.

collapse of a perfectly circular cylinder [23]. In the tracheae, we found regions where the taenidia were straight and parallel, and regions where they branched and fused together resulting in structural defects (figures 11–14). The branchings and fusions of the taenidia are likely to confer a circumferentially non-homogeneous Young's modulus to the tracheae. Through our finite element simulations, we demonstrated that the trachea with a Young's modulus which decreased by 30% in the region of highest curvature collapsed at a 0.5 kPa lower pressure than the trachea with a homogeneous Young's modulus (figure 16(g), $a/b = 1.2$). The 30% reduction in Young's modulus is likely too large to be caused by an average 12% reduction in the number of taenidia (figure 14) but, of course, this needs to be demonstrated. In comparison, we note that the buckling pressure decreased by 1.4 kPa in a tracheal tube with homogeneous Young's modulus when a/b decreased by 16% (figure 15(g)). Overall these results suggest that the cross-sectional eccentricity, more than the circumferential non-homogeneous Young's modulus, governed the collapse of the trachea (figures 15(g) and 16(g)). Therefore, we conclude that cross-sectional shape is more functionally important than taenidial bifurcation patterns in determining the collapse behavior of insect tracheal tubes.

The interaction between the tracheae and the surrounding tissues and hemolymph may also affect their *in vivo* collapse. For human pulmonary airways, for example, the surface tension at the liquid–solid interface can lead to tube collapse and airway closure, a pathological problem [24–26]. In contrast, tube collapse in the insect tracheal system provides a benefit for producing airflow. Although the insect tracheae are almost always filled with gases, liquid substances have been observed in some cases including during molting, in the presence of temperature fluctuations that induce gas condensation, or in the tracheoles [27]. These liquid substances could contribute to collapse

and, in this case, the role of other structural components of the tracheae such as the lining of the epicuticle with its hydrophobic properties (figure 8) should be investigated.

The magnitudes of buckling pressures obtained in our finite element modeling are within reason compared to pressures from real insects. Miller [28] excised a 300 μm diameter tracheal tube from the beetle *Petrognatha gigas* and experimentally determined that collapse began at pressures ranging from 0.7 to 1.3 kPa, with full collapse occurring by 2.4 kPa. A few other studies have measured the strength of pressure pulses in the hemolymph of the living insect; peaks of 0.2–0.5 kPa have been observed in pupae of the moth *Cydia pomonella* [29], 1.0–2.0 kPa in pupae of the beetle *Zophobas morio* [30], and up to 2.7 kPa in adult *Zophobas atratus* [31]. The maximum reported buckling pressures from our modeling results were roughly twice as large as these values, which may reflect morphological differences in the tracheae of these species or the possibility that collapse is not occurring under these lower pressures. Conversely, it is likely that some aspects of the collapse behavior of real tracheae are not captured by our relatively simple model. Parallel studies of tracheae and hemolymph pressures from the American cockroach need to be conducted to refine our model.

Our SEM and light microscopy studies together with the finite element simulations have advanced our knowledge of the micro-structural components of the tracheae and the possible role of the cross-sectional geometry and taenidia organization during collapse. The large thoracic tracheae considered here were likely of the elliptical collapsing type [1]. However, the rhythmic tracheal compression of these tracheae in the American cockroach has yet to be observed experimentally. With the advances in the x-ray visualization of live insects, researchers have created a detailed map of the collapsing and non-collapsing tracheae in some insect species [7]. The study by Harrison *et al* [7], and

others like it, will be of great use for performing a systematic analysis that reveals the relationship between the collapsibility of the tracheae and their microstructure. Thus the next logical step for this research will be to determine how the material design traits of collapsing tracheae compare with those of non-collapsing tracheae, or sections of tracheae that do not collapse.

Understanding how to control local collapse in a channel—including its production or prevention—is of broad interest in microfluidics [32]. Designs of networks for lab-on-a-chip or μ TAS applications are becoming increasingly sophisticated, including the use of 3D printers to more precisely dictate the shape of channels and networks [33], and the use of a broad range of materials beyond PDMS such as plastics, hydrogels, and paper [34]. Our study of insect tracheal tubes provides a new source of inspiration for such designs.

Acknowledgments

This research was supported by NSF EFRI grant #0938047 and the Virginia Tech Institute for Critical Technology and Applied Science (ICTAS). The authors thank Dr Donald E Mullins of the Department of Entomology at Virginia Tech for donating the cockroaches used in this study, and Kathy Lowe of the Morphology Laboratory at the Virginia Tech Veterinary Medicine School for preparing the tracheal specimens for SEM analysis.

References

- [1] Wigglesworth V B 1931 The respiration of insects *Biol. Rev. Camb. Philos. Soc.* **6** 181–220
- [2] Herford G M 1938 Tracheal pulsation in the flea *J. Exp. Biol.* **15** 327–38
- [3] Westneat M W, Betz O, Blob R W, Fezzaa K, Cooper W J and Lee W K 2003 Tracheal respiration in insects visualized with synchrotron x-ray imaging *Science* **299** 558–60
- [4] Socha J J, Lee W K, Harrison J F, Waters J S, Fezzaa K and Westneat M W 2008 Correlated patterns of tracheal compression and convective gas exchange in a carabid beetle *J. Exp. Biol.* **211** 3409–20
- [5] Waters J S, Lee W K, Westneat M W and Socha J J 2013 Dynamics of tracheal compression in the horned passalus beetle *Am. J. Physiol. Regul. Integr. Comp. Physiol.* **304** R621–7
- [6] Greenlee K J, Socha J J, Eubanks H B, Pedersen P, Lee W K and Kirkton S D 2013 Hypoxia-induced compression in the tracheal system of the tobacco hornworm caterpillar, *Manduca sexta* *J. Exp. Biol.* **216** 2293–301
- [7] Harrison J, Waters J, Cease A, VandenBrooks J, Callier V, Kloke C, Shaffer K and Socha J J 2013 How locusts breathe *Physiology* **28** 18–27
- [8] Babàk E 1912 Zur physiologie der atmung bei culex Mit tafel I *Intern. Revue Hydrobiol. Hydrogr.* **5** 81–90
- [9] Whitten J M 1972 Comparative anatomy of the tracheal system *Annu. Rev. Entomol.* **17** 373–402
- [10] Matusek T, Djiane A, Jankovics F, Brunner D, Mlodzik M and Mihaly J 2005 The *Drosophila* formin DAAM regulates the tracheal cuticle pattern through organizing the actin cytoskeleton *Development* **133** 957–66
- [11] Richards A G and Anderson T F 1942 Electron micrographs of insect tracheae *J. N. Y. Entomol. Soc.* **50** 147–67
- [12] Richards A G and Korda F H 1948 Studies on arthropod cuticle: II. Electron microscope studies of extracted cuticle *Biol. Bull.* **94** 212–35
- [13] Webster M R, De Vita R, Twigg J N and Socha J J 2011 Mechanical properties of tracheal tubes in the American cockroach (*Periplaneta americana*) *Smart Mater. Struct.* **20** 094017
- [14] Becker W R, Webster M R, Socha J J and De Vita R 2014 Variation in the mechanical properties of tracheal tubes in the American cockroach *Smart Mater. Struct.* **23** 057001
- [15] Williams C M 1946 Physiology of insect diapause: the role of the brain in the production and termination of pupal dormancy in the giant silkworm, *Platysamia cecropia* *Biol. Bull.* **90** 234–43
- [16] Schneider C A, Rasband W S and Eliceiri K W 2012 NIH Image to ImageJ: 25 years of image analysis *Nat. Methods* **9** 671–5
- [17] Ogden R W 1997 *Non-Linear Elastic Deformations* (New York: Dover)
- [18] Wriggers P 2008 *Nonlinear Finite Element Methods* (Berlin: Springer)
- [19] Beaulaton J 1964 Les ultrastructures des trachées et leurs ramifications dans la glande prothoracique du ver à soie Tussor (*Antheraea pernyi* Guer. Lepidoptère, Attacide) *J. Microscopie* **3** 91–104
- [20] Whitten J M 1976 Stage specific larval, pupal, and adult cuticles in the tracheal system of *Sarcophaga bullata* *J. Morphol.* **150** 369–97
- [21] Schutten W H and van Horn D L 1980 Corneal endothelial cell shrinkage after critical point drying *Ann. Ophthalmol.* **12** 1165–7
- [22] Timoshenko S P and Gere J M 2012 *Theory of Elastic Stability* (New York: Dover)
- [23] Simitses G J 1986 Buckling and postbuckling of imperfect cylindrical shells: a review *Appl. Mech. Rev.* **39** 1517–24
- [24] Hazel A L and Heil M 2005 Surface-tension-induced buckling of liquid-lined elastic tubes: a model for pulmonary airway closure *Proc. R. Soc. A* **461** 1847–68
- [25] Heil M 1999 Airway closure: occluding liquid bridges in strongly buckled elastic tubes *Trans. ASME, J. Biomech. Eng.* **121** 487–93
- [26] Rosenzweig J and Jensen O E 2002 Capillary-elastic instabilities of liquid-lined lung airways *Trans. ASME, J. Biomech. Eng.* **124** 650–5
- [27] Förster T D and Wood H A 2013 Mechanisms of tracheal filling in insects *Biol. Rev.* **88** 1–14
- [28] Miller P L 1966 The supply of oxygen to the active flight muscles of some large beetles *J. Exp. Biol.* **45** 285–304
- [29] Slama K and Neven L 2001 Active regulation of respiration and circulation in pupae of the codling moth (*Cydia pomonella*) *J. Insect Physiol.* **47** 1321–36
- [30] Pendar H, Kenny M C and Socha J J 2015 Tracheal compression in pupae of the beetle *Zophobas morio* *Biol. Lett.* **11** 20150259
- [31] Ichikawa T 2008 Periodic abdominal pumping supports leg development during metamorphosis in tenebrionid beetle *Zophobas atratus* *Comp. Biochem. Physiol. A Mol. Integr. Physiol.* **150** 8–13
- [32] Kleinstreuer C 2013 *Microfluidics and Nanofluidics: Theory and Selected Applications* (New York: Wiley)
- [33] Ho C M B, Ng S H, Li K H H and Yoon Y J 2015 3D printed microfluidics for biological applications *Lab Chip* **15** 3627–37
- [34] Ren K, Chen Y and Wu H 2014 New materials for microfluidics in biology *Curr. Opin. Biotech.* **25** 78–85
- [35] Amestoy P R, Duff I S and L'Excellent J Y 2000 Multifrontal parallel distributed symmetric and unsymmetric solvers *Comput. Methods Appl. Mech. Eng.* **184** 501–20